IEEE Open Journal of
Antennas and Propagation

Received 26 January 2023; revised 28 February 2023; accepted 4 March 2023. Date of publication 16 March 2023; date of current version 7 April 2023.

Digital Object Identifier 10.1109/OJAP.2023.3258147

Additive Manufacturing of Linear Continuous Permittivity Profiles and Their Application to Cylindrical Dielectric Resonator Antennas

SIMON P. HEHENBERGER[1,2] (Student Member, IEEE), STEFANO CAIZZONE[1] (Member, IEEE), AND ALEXANDER G. YAROVOY[2] (Fellow, IEEE)

[1]Institute for Communication and Navigation, German Aerospace Center, 82234 Wessling, Germany

[2]Microwave Sensing, Signals and Systems, TU Delft, 2628 CD Delft, The Netherlands

CORRESPONDING AUTHOR: S. P. HEHENBERGER (e-mail: simon.hehenberger@dlr.de)

ABSTRACT The utilization of additive manufacturing (AM) to engineer the permittivity profile of dielectric resonator antennas (DRAs) is considered. For the first time, the capabilities of AM are exploited to create continuously swept permittivity profiles and applied to cylindrical DRAs. The spatial variant lattices (SVL) synthesis algorithm is implemented to create the desired permittivity profiles from a single material, and resulting geometries are manufactured using a high-permittivity material in a fused deposition modeling AM process. Three individual antennas for global navigation satellite system bands are designed and manufactured, two inhomogeneous DRAs with continuous permittivity profiles along the radial and vertical axis, and one homogeneous DRA for comparison. The manufactured antennas are characterized by impedance, realized gain, and axial ratio. Experimental results agree well with simulations and show increased impedance-, gain-, and axial-ratio bandwidths for both inhomogeneous antennas compared to the homogeneous one.

INDEX TERMS 3D printing, additive manufacturing, dielectric crystals, dielectric resonator antenna, inhomogeneous permittivity, spatially varried lattices.

I. INTRODUCTION

DIELECTRIC resonator antennas (DRAs) are viable alternatives to traditionally employed radiating elements such as wire and patch antennas thanks to their high radiation efficiency due to the absence of conduction losses [1]. Depending on the design approach DRAs provide appealing gain, bandwidth, and polarization characteristics due to their versatility in shape, dielectric characteristics, and feeding mechanism [2], [3]. Furthermore, DRAs offer great potential for the miniaturization of antenna elements as their size is inversely proportional to the square root of the resonating body's relative permittivity. Thorough reviews of DRA technology highlighting historical developments and recent advancements are presented in [4], [5]. Multi-permittivity and inhomogeneous variations of the dielectric resonator are thought to be a proper way to achieve wideband operation [6], [7], [8], multiband behavior [9] or increase the spurious-free window [10]. These inhomogeneous DRAs are usually manufactured by either milling perforations into the resonator or stacking (gluing) different materials together. Alternatives to these methods are desired since the milling process is limited concerning complex internal features, and the utilization of glues is cumbersome and introduces an additional possible uncertainty source. Accompanying the developments in DRA technology, advances in additive manufacturing (AM) have exploded during the last decade. This is especially interesting concerning DRAs since AM allows the manufacturing complex dielectric structures with relatively low-cost machines and processes. Several works successfully utilized AM of dielectrics to create bulk homogeneous DRAs with various materials and shapes [11], [12], [13]. Furthermore, the AM capabilities have been exploited to create complex periodic distributions of high-permittivity material to engineer the permittivity of a

DRA [14]. Additionally, multi-permittivity (inhomogeneous) DRAs have been created for bandwidth improvement [15], [16], [17], [18]. Additive manufacturing of multi-permittivity devices has also been successfully employed to create flat lenses [19]. However, so far, additively manufactured devices with inhomogeneous permittivity have only been manufactured with discrete sections of a specific permittivity. The potential of continuously swept permittivity distributions in the device has yet to be explored in literature. This work aims to address this literature gap by utilizing spatial variant lattices (SVL), as introduced in [20], to create periodically structured geometries with continuously varied volumetric fill-fraction. The goal is to show the design, simulation, and manufacturing of swept permittivity profiles and investigate their effect on the performance of cylindrical DRAs. For this purpose, linearly swept profiles with increasing permittivity along the radial and vertical axis are studied. Earlier studies on DRA with piece-wise constant permittivity profiles inspire this choice for the selected permittivity profiles, and this work focuses instead on demonstrating the feasibility of precisely manufacturing a continuous swept profile, thus enabling future research about an ad-hoc-optimization of a DRAs permittivity profile. The antennas discussed in this work are intended for applications with global navigation satellite systems (GNSS) and optimized for operation at the Galileo E1 band center frequency of 1.575 GHz. However, the proposed approach for creating continuously swept permittivity profiles can be scaled to any desired frequency band, given that the manufacturing process can produce structures sufficiently small with respect to the wavelength. The rest of the paper is structured as follows. Section II explains the DRA concept, the selected permittivity profiles, and the utilized face-centered cubic (FCC) unit cell design based on spatial harmonics. Furthermore, the approach to varying the effective permittivity throughout the DRAs resonating body is explained, and an example of a lattice with a swept volumetric infill is presented. Section III presents the optimization results to find the appropriate dimensions for DRAs with linearly swept effective permittivity profiles along their radial and vertical axis for operation at the E1 band (1.575 GHz). Insight into the manufacturing process and measurement results are presented in Section IV. Furthermore, a discussion and a conclusion are given in Sections V and VI, respectively.

II. ANTENNA CONCEPT

A. ANTENNA GEOMETRY AND PERMITTIVITY RANGE

The individual cylindrical DRAs with radius a, height h on a cylindrical ground plane with radius a_{GP}, as depicted in Figure 1, are fed via two 50 Ω coaxial probes of length l_{feed} with an offset of a_{feed} from the DRA center. The probes are excited with 90° phase offset (Port 1: 0°; Port2: −90°) for right-hand circular polarization (RHCP). The antennas are manufactured via a fused deposition modeling (FDM) process utilizing the ABS1500 filament from Avient (former Preperm) with a nominal relative permittivity of $\varepsilon_{\mathrm{r,n}} = 15$.

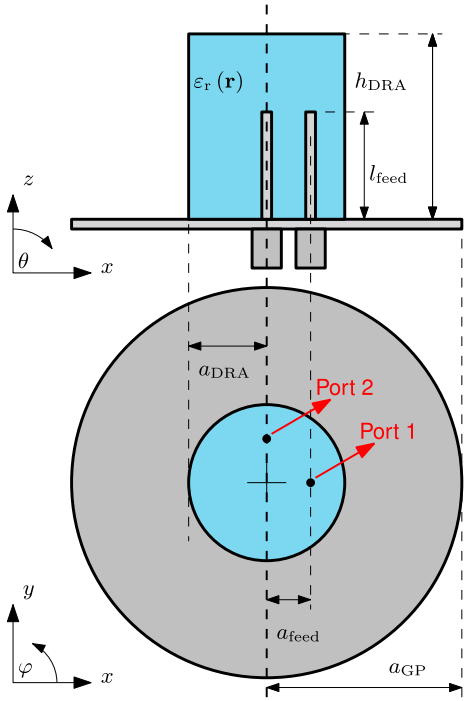

FIGURE 1. The geometry of the cylindrical dielectric resonator antenna with two coaxial probe feeds mounted on a cylindrical ground plane.

However, the relative permittivity of printed substrates heavily depends on the FDM process parameters like layer height, line width, extrusion multiplier, etc., as demonstrated in [21]. Therefore, the effect of the later utilized printing parameters on the relative permittivity of a printed bulk ABS1500 sample was investigated with a material characterization setup based on rectangular waveguides as described in [22]. The experiment showed a reduction in relative permittivity from the nominal value to $\varepsilon_{\mathrm{r,max}} = 13.7$, which is further considered to be the maximum achievable permittivity in our design. The swept permittivity profiles are generated via the method introduced in [20], based on an FCC unit cell generated via spatial harmonics as described in [24]. The effective permittivity of the unit cell can be adjusted with the threshold values *th*, which controls the volumetric infill, as further explained below.

B. UNIT CELL DESIGN

In contrast to other works where unit cells are parametrically defined [14], [23], this work takes a different approach and defines unit cells via spatial harmonics along the reciprocal lattice vectors of the desired crystal geometry as described in [24]. Face-centered cubic unit cell symmetry was chosen in this work as it allowed for easier manufacturing. The approach via spatial harmonics allows the straightforward application of the algorithm discussed in [20], which is later used to introduce the swept permittivity profile. The unit cell is defined with its lattice constant a and primitive lattice vectors of the FCC symmetry $\mathbf{t}_1 = \frac{a}{2}[0\ 1\ 1]^{\mathrm{T}}$, $\mathbf{t}_2 = \frac{a}{2}[1\ 0\ 1]^{\mathrm{T}}$ and $\mathbf{t}_3 = \frac{a}{2}[1\ 1\ 0]^{\mathrm{T}}$ which point from the current lattice node

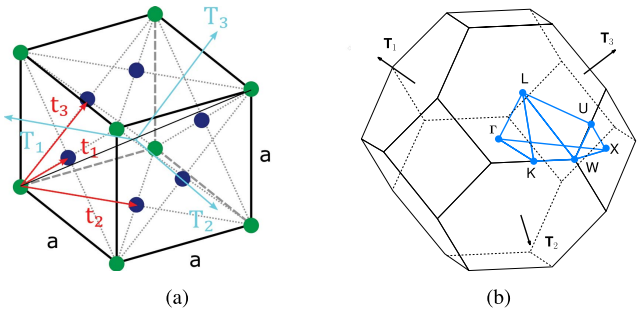

FIGURE 2. Face-centered cubic crystal (a.) symmetry with lattice constant *a*, primitive lattice vectors t_1, t_2 and t_3 and reciprocal lattice vectors T_1, T_2 and T_3; (b.) Brillouin zone with key points of symmetry.

to its three nearest neighbors, as depicted in Figure 2. For each set of two primitive lattice vectors, a perpendicular reciprocal lattice vector can be found via

$$\mathbf{T}_1 = 2\pi \frac{\mathbf{t}_2 \times \mathbf{t}_3}{\mathbf{t}_1 \cdot (\mathbf{t}_2 \times \mathbf{t}_3)} \tag{1}$$

$$\mathbf{T}_2 = 2\pi \frac{\mathbf{t}_3 \times \mathbf{t}_1}{\mathbf{t}_1 \cdot (\mathbf{t}_2 \times \mathbf{t}_3)} \tag{2}$$

$$\mathbf{T}_3 = 2\pi \frac{\mathbf{t}_1 \times \mathbf{t}_2}{\mathbf{t}_1 \cdot (\mathbf{t}_2 \times \mathbf{t}_3)} \tag{3}$$

where the magnitude describes the periodicity of the lattice.

The lattice geometry in the respective Bravais lattice is based on a superposition of N spatial harmonics with individual grating vectors $\mathbf{g}_i$, $i = 1, \ldots, N$,

$$A = \sum_{i=1}^{N} A_i e^{J\left(g_{i,x}x + g_{i,y}y + g_{i,z}z\right)} \tag{4}$$

where A is a complex valued function in terms of spatial coordinates x, y, and z.

By choosing the individual grating vectors, $\mathbf{g}_i$ such that they are oriented along the reciprocal lattice vectors $\mathbf{T}_i$ as defined in (3), and their periodicity is an integer multiple of the lattice periodicity, the superposition of spatial harmonics will obtain the respective crystal symmetry and periodicity. Before generating the unit cell geometry a min-max feature scaling is applied on the real part of the superimposed spatial harmonics A as an intermediate step

$$\tilde{A} = \frac{\mathrm{Re}\{A\} - \min(\mathrm{Re}\{A\})}{\max(\mathrm{Re}\{A\}) - \min(\mathrm{Re}\{A\})} \tag{5}$$

with $\tilde{A}$ now representing a real function in terms of spatial coordinates x, y, and z with values between 0 and 1. The overall unit cell UC is computed, for some threshold $th \in [0\ 1]$, via

$$UC := \tilde{A} \geq th \tag{6}$$

where th represents an the value of an isosurface throughout the unit cell. Regions where $\tilde{A} \geq$ are further considered to consist of material 1 (in our case the 3D printed substrate) and regions where $\tilde{A} < th$ are considered to consist of material 2 (in our case free space). Figure 3 shows individual

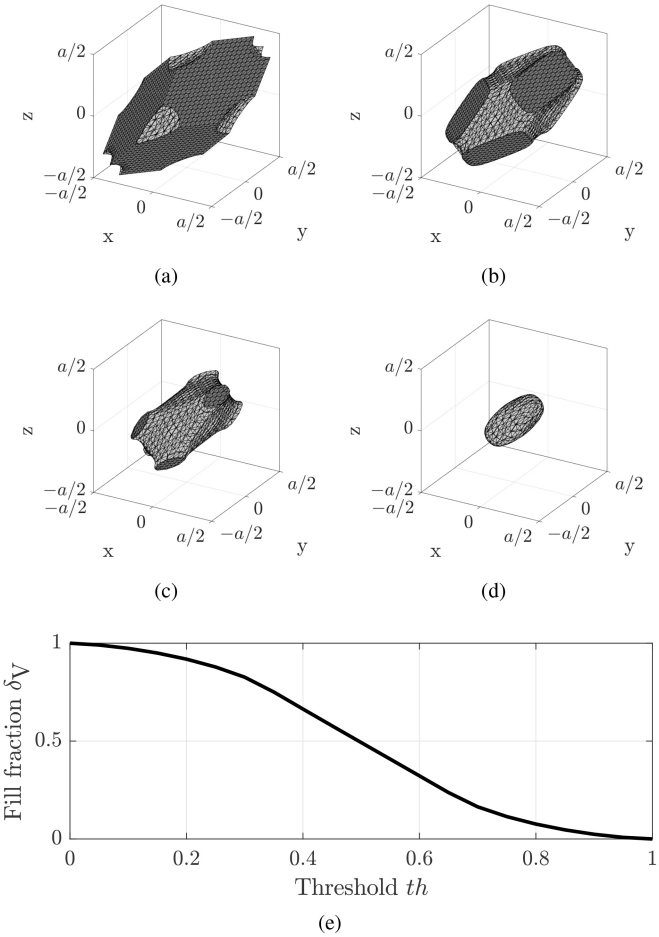

FIGURE 3. Unit-cells created via a threshold parameter *th* based on superimposed spatial harmonics in the direction of the reciprocal lattice vectors of the FCC crystal geometries (a) $th = 0.2$; (b) $th = 0.4$; (c) $th = 0.6$; (d) $th = 0.8$. The faces touching the boundaries of the crystal unit cell are shaded darker than faces that do not. (e) Relationship between the volumetric infill fraction and the threshold parameter.

unit cells with FCC symmetry with different thresholds created with $N = 3$ equal amplitude spatial harmonics and grating vectors equal to the FCC reciprocal lattice vectors. The benefit of utilizing spatial harmonics to create the unit cell geometry is that one can easily vary the fill fraction δ_V by adjusting the inverse proportionally related threshold value th. Furthermore, the utilization of spatial harmonics allows the straightforward and computationally efficient application of the algorithm introduced in [20] to create swept permittivity profiles, as is further discussed below in Section II-E.

C. EFFECTIVE PERMITTIVITY

The relationship between the unit cell threshold th and its effective permittivity is not trivial and such relationships are usually studied with effective media theories. The Maxwell Garnett Approximation (MGA) [25] has been especially prominent for modeling the effective permittivity of additive manufactured dielectrics. However, several studies have shown that the MGA lacks accuracy when applied to

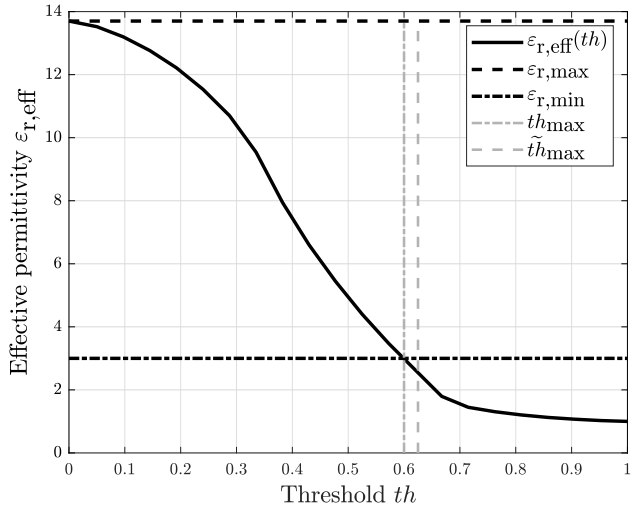

FIGURE 4. Relationship between the unit cell threshold (th) and the effective permittivity for a face-centered cubic dielectric crystal created from a material with permittivity $\varepsilon_r = 13.7$. The lattice is fully connected up to a maximum threshold $\tilde{th}_{max}$ and is compatible to our manufacturing process up to th_{max}.

high volumetric infill fractions and moderate dielectric contrasts [26]. The plane wave expansion method (PWEM) [27] is a suitable alternative to the MGA to compute the effective permittivity of additive manufactured dielectric unit cells [22], [28]. The method discretizes Maxwells equations with periodic boundary conditions on a plane wave basis. Given the permittivity distribution of the unit cell $\varepsilon_{r,uc}(\mathbf{r})$ and a Bloch wave vector $\boldsymbol{\beta}$ the PWEM computes the modes (eigenvectors) that fit the phase boundary condition imposed by the chosen Bloch vector $\boldsymbol{\beta}$ and their respective wavenumbers k_0 (eigenvalues). A complete analysis of the crystal with this method requires a dense sampling of Bloch vectors in the Brillouin zone of the crystal (Figure 2), which is computationally demanding. However, we are only concerned with the effective permittivity in the long wavelength limit, which corresponds to low-magnitude Bloch wave vectors (Bloch vectors around the Γ key point of symmetry). We can extract the effective refractive index n_{eff} of the fundamental mode via

$$n_{eff} = \frac{|\boldsymbol{\beta}|}{k_0} = \sqrt{\varepsilon_{r,eff}\mu_r} \tag{7}$$

which for purely dielectric media ($\mu_r = 1$), is the square root of the effective permittivity $\varepsilon_{r,eff}$.

This method is now used to compute the effective permittivity of FCC unit cells made from a material with permittivity $\varepsilon_{r,max}$ with different thresholds th as depicted in Figure 3. The effective permittivity as a function of the threshold th is depicted in Figure 4. The lattice is connected to its neighboring unit cell up to a maximum threshold of $\tilde{th}_{max} = 0.625$, and for convenient manufacturing, a maximum threshold of $th_{max} = 0.6$ was chosen which corresponds to a minimum manufacturable effective relative permittivity of $\varepsilon_{r,min} = 3$, which is further considered to be the minimum achievable permittivity in our design.

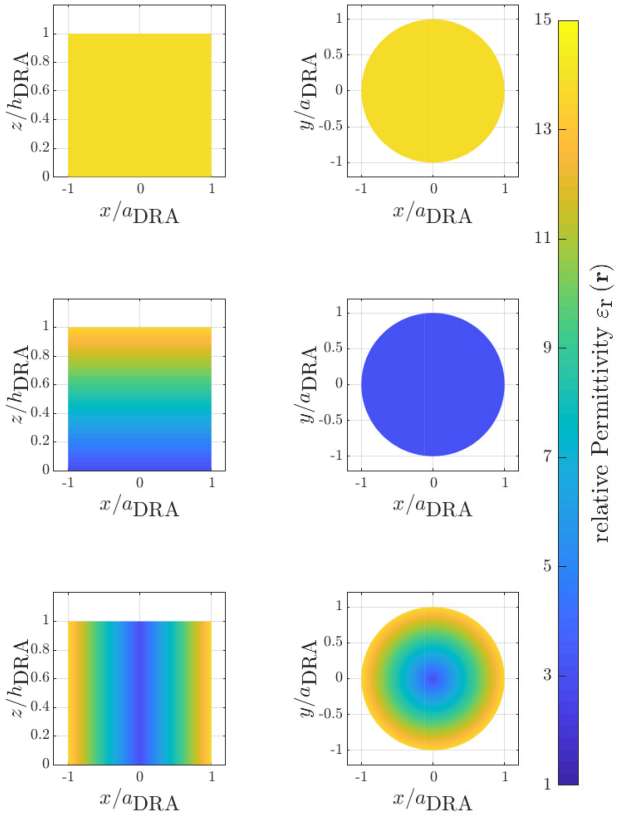

FIGURE 5. Permittivity profile cuts of the considered homogeneous (top), inhomogeneous along the vertical axis (middle) and inhomogeneous along the radial axis (bottom) DRAs at $y = 0$ (left) and $z = 0$ (right).

D. PERMITTIVITY PROFILES

Three individual cylindrical DRA versions with different permittivity profiles $\varepsilon_r(\mathbf{r})$, based on the geometry depicted in Figure 1 are considered in this work. A homogeneous DRA is manufactured with the maximum achievable relative permittivity while two inhomogeneous DRAs are engineered to obtain a linearly swept permittivity profile from $\varepsilon_{r,min}$ to $\varepsilon_{r,max}$. The individual DRAs will further be referred to as:

- *DRA-H* - Homogeneous DRA with $\varepsilon_r(\mathbf{r}) = \varepsilon_{r,max}$ for comparison purposes;
- *DRA-IHZ* - Inhomogeneous DRA with a linearly swept permittivity profile along the vertical (z)-axis, $\varepsilon_r(\mathbf{r}) = k_z z + d$;
- *DRA-IHR* - Inhomogeneous DRA with a linearly swept permittivity profile along the radial (r)-axis, $\varepsilon_r(\mathbf{r}) = k_r r + d = k_r\sqrt{x^2 + y^2} + d$;

with

$$k_z = \frac{\varepsilon_{r,max} - \varepsilon_{r,min}}{h_{DRA}} \tag{8}$$

$$k_r = \frac{\varepsilon_{r,max} - \varepsilon_{r,min}}{a_{DRA}} \tag{9}$$

$$d = \varepsilon_{r,min}. \tag{10}$$

The individual permittivity profiles of the three considered DRA configurations are depicted in Figure 5.

E. SPATIAL VARIED LATTICES

The idea of utilizing a spatial variation of dielectric infill to introduce inhomogeneous effective permittivity for design purposes is not new. A common planar design approach is utilizing space-filling curves with modulated trace thickness [29] to achieve spatial-dependent material responses. However, space-filling curves are challenging to adapt to 3D geometries. 3D spatial variation has been introduced with voxelated approaches where parametrically defined unit cells are treated like individual voxels, which have a practical permittivity value assigned that is engineered by changing the geometric parameters of the unit cell. Another popular method is to create sections in a lattice that will be printed with different materials or infill fractions, as shown in [19]. Here we utilized the less known but powerful algorithm to synthesize spatially variant lattices (SVL) as introduced in [20]. The details of the SVL algorithm are not repeated here. Roughly explained, the approach decomposes a given unit cell into spatial harmonics and applies spatial variations like rotations or changes in the lattice period onto these individual harmonics. Later the whole lattice is assembled by the superposition of the individual harmonics, which results in a continuous and smooth structure with minimum deformation to individual unit cells. The SVL algorithm, although computationally expensive, offers a powerful tool to influence dielectric crystal lattices in numerous ways. Due to the computationally demanding nature of the SVL algorithm we utilize the spatial harmonics approach to design a unit cell rather than decomposing an arbitrary unit-cell geometry in a large number of spatial harmonics. The spatial harmonics design approach enables us to create a fully 3D periodic unit cell via only $N = 3$ spatial harmonics resulting in a manageable computation time when applying the SVL algorithm. Figure 6 depicts a cuboid consisting of $1 \times 1 \times 10$ unit cells, where the SVL algorithm is employed to continuously sweep the fill fraction of the FCC unit cell along the z-axis.

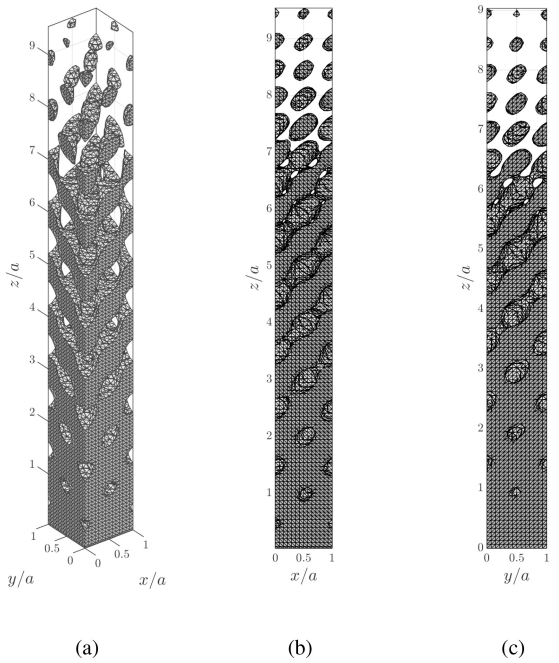

FIGURE 6. Example of a face-centered cubic dielectric crystal lattice with linearly swept volumetric fill fraction. (a) 3D-view, (b) *xz*-plane, (c) *yz*-plane.

TABLE 1. Geometric parameters of DRA antennas and permittivity function $\varepsilon_r(\mathbf{r})$ after optimization with the goal obtain a minimum in the reflection coefficient at the design frequency 1.575 GHz.

DRA (units in mm)	a	h	a_{feed}	l_{feed}	$\varepsilon_r(\mathbf{r})$
DRA - H	22.85	33.00	12.95	22.45	13.7
DRA - IHZ	27.75	38.85	16.15	20.10	$0.275z$+3
DRA - IHR	22.80	34.29	13.10	19.30	$0.469r$+3

III. DESIGN AND SIMULATION

While the homogeneous DRA dimensions can be found quickly utilizing the design equations in [30], no such equations are available for inhomogeneous DRAs. Therefore, the dimensions of the two inhomogeneous antenna variations are found via optimization in the commercial EM solver package Ansys high-frequency structure simulation software (HFSS). Since HFSS does not allow the definition of inhomogeneous material, the model for the inhomogeneous DRAs is built with distinct layers or shells of homogenous material to approximate the desired permittivity profile in the resonating body, as depicted in Figure 5. While the range of the permittivity profile is fixed form $\varepsilon_r \in [3\ 13.7]$ as explained above, the model geometry is subject to an optimization problem to match the antenna to the center frequency of the E1 GNSS band (1.575 GHz). The optimization is set up to minimize the reflection S_{11} and transmission S_{21} at the E1 center frequency by changing the geometric parameters a_{DRA}, h_{DRA}, a_{feed} and l_{feed}. It has been observed that the results obtained from the simulations sufficiently converged around 20 shells and layers. Therefore, the optimization routine was carried out with 20 individual shells/layers, and for the final simulations, this number was increased to 50. While Table 1 lists the optimized geometry parameters for each of the three antenna variations with their respective permittivity function $\varepsilon_r(\mathbf{r})$, the resulting reflection coefficients, realized gain, and the axial ratio at $\theta = 0°$ are plotted as a function of frequency in Figures 7 and 8, respectively. In Figure 7 one can observe that the reflection coefficients show respective minima approximately at the E1 center frequency, as was the goal of the optimization. Furthermore, both inhomogeneous DRAs extend the impedance bandwidth with respect to the homogeneous one. An interesting observation is that the coupling between the two feed ports is reduced for the inhomogeneous DRAs at the design frequency, which implies improved realized gain and axial ratio values, which is confirmed by the plots in Figure 8.

IV. MANUFACTURING AND MEASUREMENTS

The geometric mesh of the continuously varied lattice for the inhomogeneous DRAs is obtained directly from the

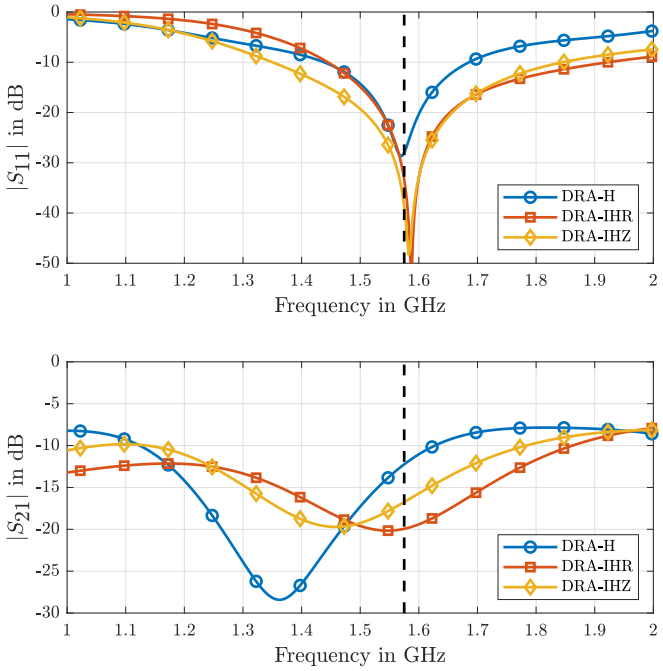

FIGURE 7. Simulated S-parameters of the homogeneous (blue), radial inhomogeneous (red), and vertical inhomogeneous (yellow) cylindrical dielectric resonator antennas between the two feeding probes. (top) S_{11}; (bottom) S_{21}.

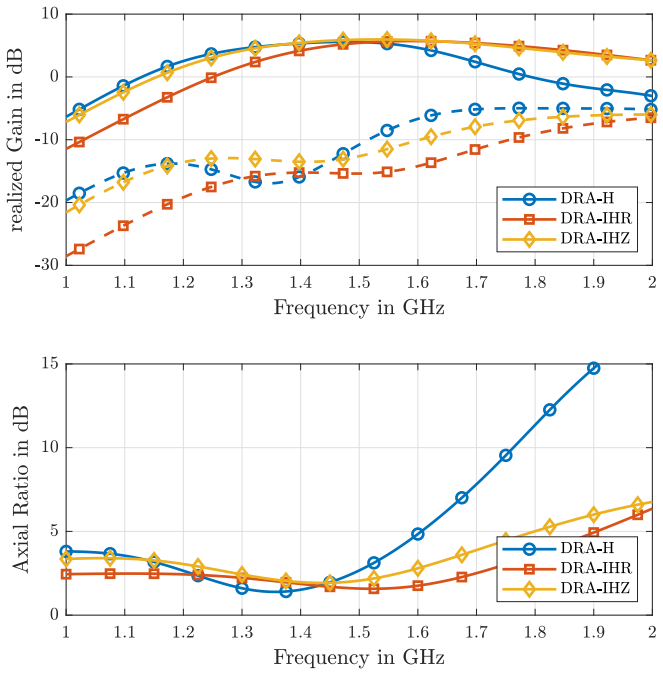

FIGURE 8. Simulated RHCP (solid) and LHCP (dashed) realized gain (top) and axial-ratio (bottom) at $\theta = 0°$ as a function of frequency for the homogeneous (blue), radial inhomogeneous (red), and vertical inhomogeneous (yellow) cylindrical dielectric resonator antennas.

SVL algorithm and saved as a standard tessellation language (STL) file. Individual STL files are prepared for printing via the PrusaSlicer v2.5.0 which translates the antenna geometries into G-code for the respective manufacturing machine. Models are printed with 100% infill,

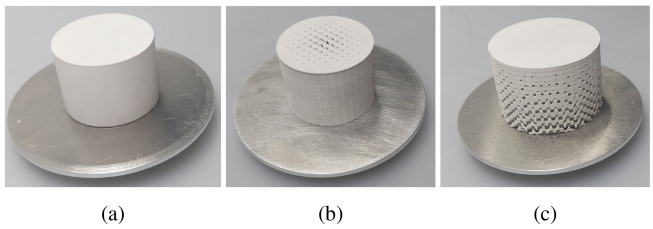

FIGURE 9. Manufactured DRA antennas with different permittivity profiles (a) homogeneous (DRA-H); (b) linear permittivity profile, increasing in the radial direction (DRA-IHR); (c) linear permittivity profile, increasing along the vertical axis (DRA-IHZ).

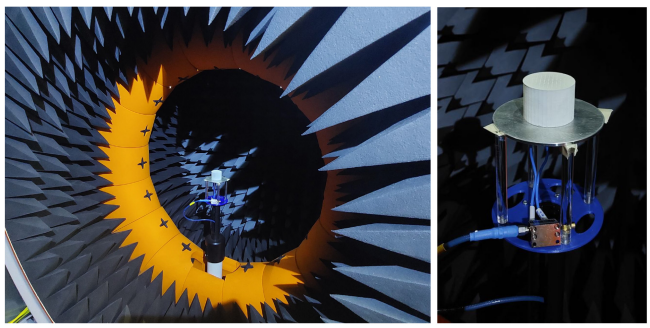

FIGURE 10. MVG Starlab 6 GHz near-field measurement chamber. (a) Setup; (b) Setup (detailed) DRA-IHR with 90° hybrid for RHCP polarization.

employing a heavily customized 3D printer based on the E3D tool changer with the ABS1500 filament from Preperm. We utilize a 0.25mm nozzle at an extrusion temperature of 250° Celsius with a heated bed at 110° Celsius and a layer height of 0.15mm.[1] The finished antennas with installed coaxial probes and mounted on individual aluminum ground planes are depicted in Figure 9. Scattering parameters between the two feed-ports were measured with a vector network analyzer between 1 and 2 GHz and are compared to the simulation results in Figure 11. For the measurement of the DRAs radiation patterns, the individual antennas are fed via a 90° hybrid (MiniCircuits ZX10Q-2-19+) for RHC polarization and placed in an MVG Starlab near-field chamber as shown in Figure 10. Measured realized gain in RHC and LHC polarization values at $\theta = 0°$, as well as the axial ratio at $\theta = 0°$, are plotted as a function of frequency in Figure 12 and compared to simulated results. The simulated and measured realized gain and axial ratio patterns at the design frequency are compared for the DRA-H, DRA-IHR, and DRA-IHZ in Figures 13, 14 and 15 respectively. Simulated and measured numerical values of impedance bandwidth, axial ratio bandwidth, and realized gain are compared for each of the three antennae in Table 2. From Figure 11 one is able to observe some discrepancies between simulation and measurement. First of all, the homogeneous antenna obtains a broader impedance bandwidth

1. The printing parameters are the same used for manufacturing the bulk sample which was measured to obtain a permittivity of $\varepsilon_{r,max} = 13.7$, as explained in Section II-A.

TABLE 2. Comparison of simulated and measured results for the resonance frequency f_{res}, impendence bandwidth B_Z, axial ratio bandwidth B_{AR} and realized gain G_r of the DRA antennas.

DRA	source	f_{res} in GHz	B_Z ($S_{11} < -10$dB)		B_{AR} (3dB; $\theta = 0$)		G_r ($\theta = 0$; $f = 1.575$ GHz)	
			in MHz	in %	in MHz	in %	RHC in dB	LHC in dB
DRA-H	sim	1.575	245	15.7	353	26.3	5.0	-7.5
DRA-H	meas	1.591	457	28.7	425	29.8	4.3	-15.3
DRA-IHR	sim	1.582	475	28.2	790	58.7	5.71	-14.7
DRA-IHR	meas	1.794	513	28.6	549	32.1	4.1	-16.5
DRA-IHZ	sim	1.580	495	30.9	410	29.9	5.9	-10.8
DRA-IHZ	meas	1.631	384	23.5	355	21.4	4.8	-14.8

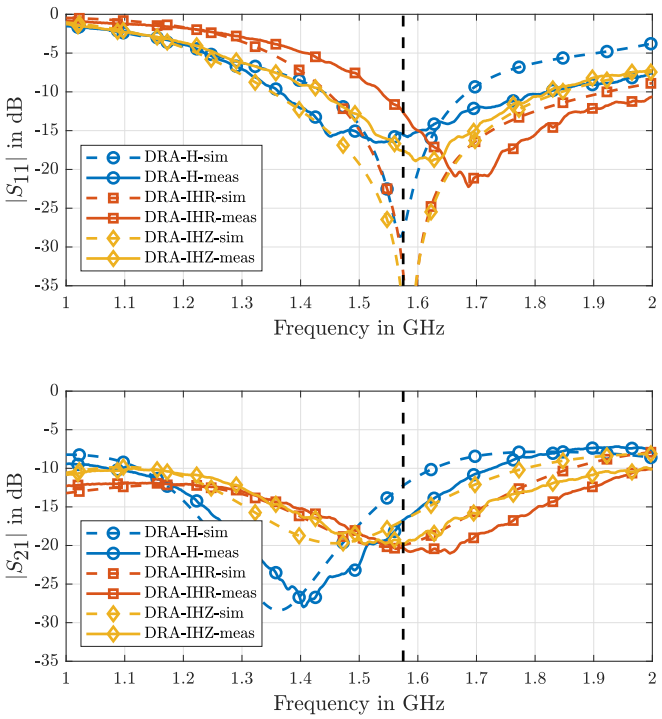

FIGURE 11. Comparison of measured (solid) and simulated (dashed) S-parameters of the homogeneous (blue), radial inhomogeneous (red), and vertical inhomogeneous (yellow) cylindrical dielectric resonator antennas between the two feeding probes. (top) S11; (bottom) S21.

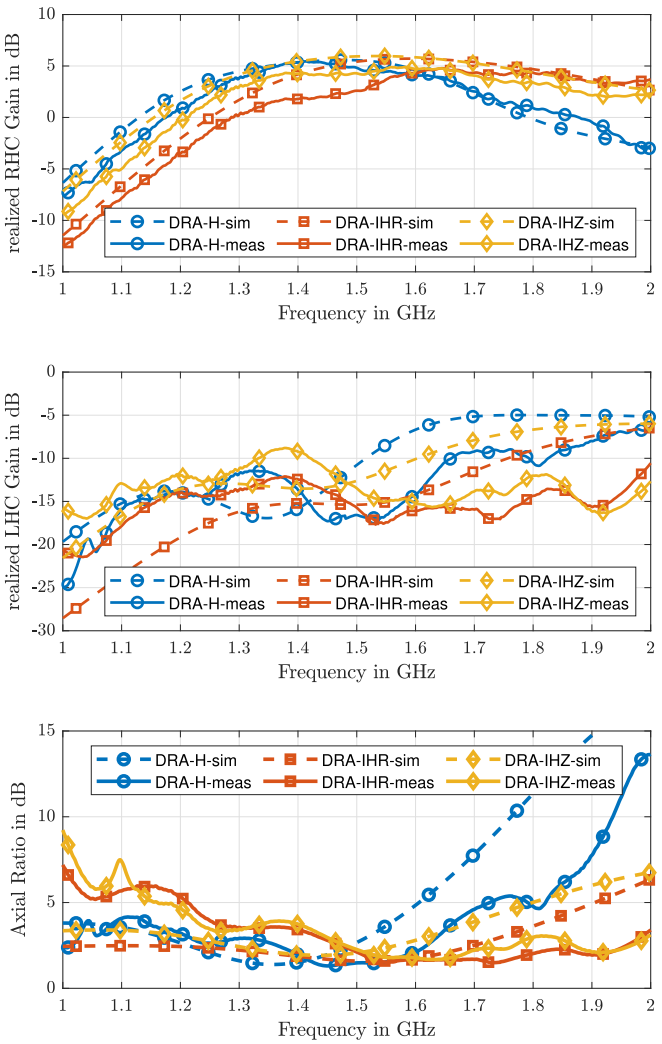

FIGURE 12. Comparison of measured (solid) and simulated (dashed) RHCP realized gain (top), LHCP realized gain (middle), and axial ratio (bottom) of the homogeneous (blue), radial inhomogeneous (red) and vertical inhomogeneous (yellow) cylindrical dielectric resonator.

than predicted from simulations. Furthermore, the reflection coefficients for the DRA-IHR and DRA-IHZ antennae do not obtain their respective minima at the design frequency but are shifted to higher frequencies. Although there are some shifts in the center frequency, the predicted effect of improved isolation between the feed ports is confirmed for both the DRA-IHR and DRA-IHZ antennas.

The measured RHC realized gains of the DRA-H, DRA-IHR, and DRA-IHZ antennas in Figure 12 show slightly reduced values compared to the simulated ones, which can be explained via the insertion loss of the utilized 90° hybrid that was employed to achieve RHC polarized radiation. Additionally, the realized gain of the DRA-IHR antenna shows a more significant reduction in realized Gain between 1.35 and 1.55 GHz compared to simulation which most probably due to the shifted resonance frequency of the DRA-IHR antenna. The predicted improvement of axial ratio values at $\theta = 0°$ is well observed in measurement in Figure 12 (bottom) for both inhomogeneous DRAs. However, the shape of the axial

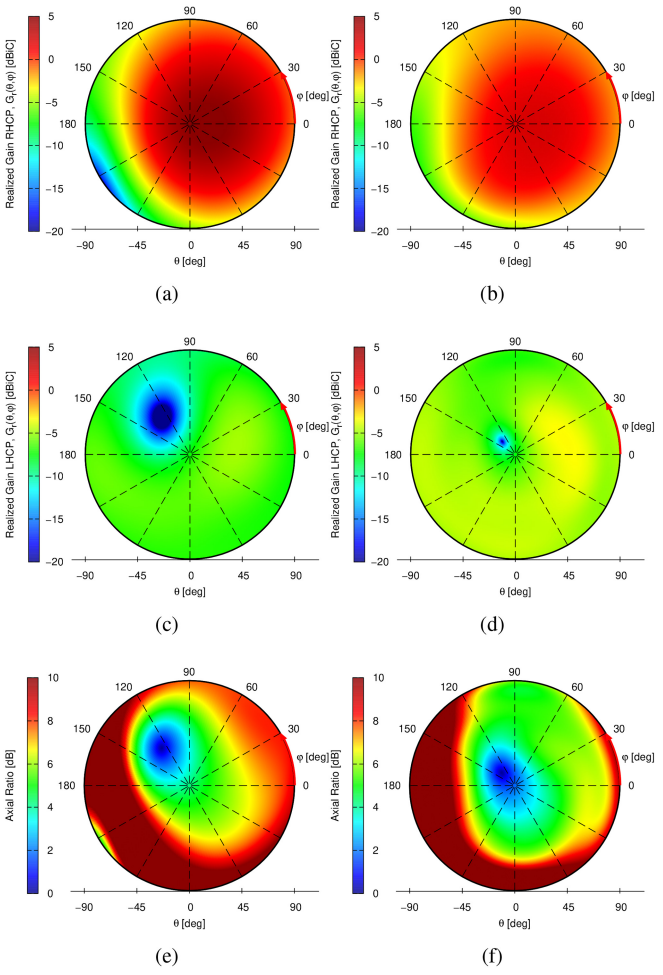

FIGURE 13. RHCP realized gain (a,b), LHCP realized Gain (c,d), and axial ratio (e,f), simulation (left) and measurement (right) results of the homogeneous DRA at E1 center frequency (1.575 GHz).

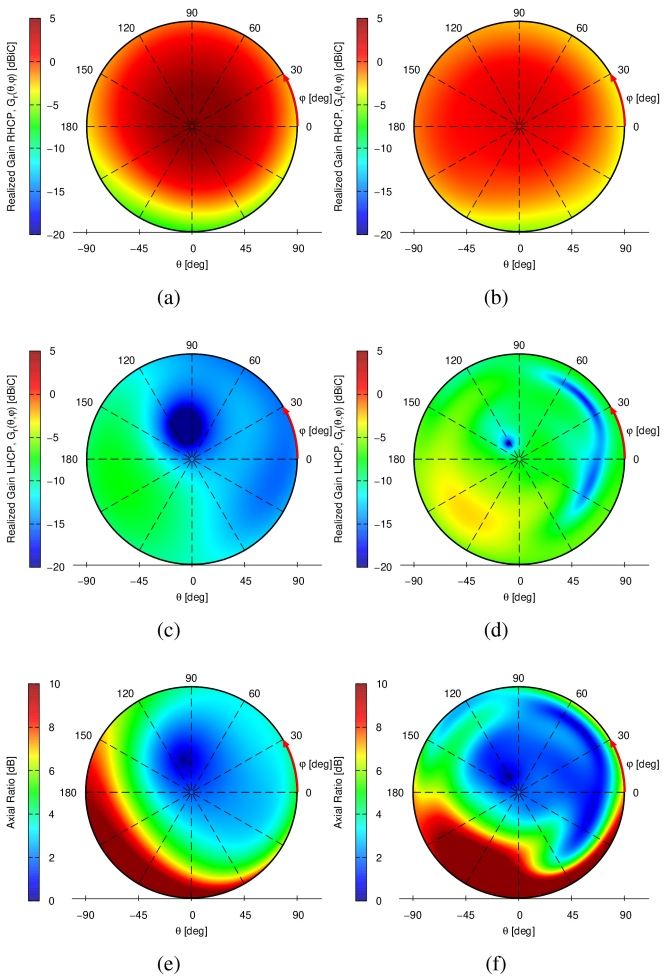

FIGURE 14. RHCP realized gain (a,b), LHCP realized Gain (c,d) and axial ratio (e,f), simulation (left) and measurement (right) results of the inhomogeneous DRA with a linear permittivity profile along the radial axis at E1 center frequency (1.575 GHz).

ratio curves is shifted to higher frequencies similar to the shift observed in the feed coupling $|S_{21}|$ in Figure 11.

The realized gain and axial ratio patterns at 1.575 GHz depicted in Figures 13, 14, and 15 are not perfectly symmetric as the azimuth region $\varphi \in [0^\circ\ 90^\circ]$ experiences higher RHC realized gain and improved axial ratio values. This effect is due to the position of the two coaxial feed probes at $\varphi = 0^\circ$ and $\varphi = 90^\circ$ as shown in the schematic of the antenna in Figure 1. This distortion can be improved by further increasing the number of feed points of the individual antennas. Overall the shape of the realized gain and axial ratio patterns predicted by simulations is adequately reproduced in the measurement. The inhomogeneous DRAs show significantly improved axial ratio values, not only at $\theta = 0^\circ$ but also over a larger angular area compared to the homogeneous DRA due to the reduced feed coupling in the inhomogeneous resonator bodies.

V. DISCUSSION

Generally, the chosen simulation approaches deliver a reasonable agreement between simulations and measurements. This fact is essential to highlight due to two reasons. First, the modeling of the relationship between the volumetric fill-fraction and effective permittivity of the unit cell is done with the plane wave expansion method, which assumes a plane wave propagating through the infinite lattice, while the DRA feeding can be considered to be more of a point-like source. The point-like source excites a broad spectrum of homogeneous and inhomogeneous spectral harmonics of the electromagnetic field. Nevertheless, the results are in reasonable agreement confirming the validity of the PWEM modeling approach. Another reason is that the numerical simulation model of the DRA is not considered with the final geometry of the DRA but with individual layers and shells of homogeneous dielectrics. The layered/shelled approach was chosen because the spatial harmonic design approach cannot be replicated in HFSS. However, still, a high number of layers/shells is necessary for the model to adequately represent the intended permittivity profile, leading to a rather complex mesh and significantly increased simulation times. The observed improvement in the operational bandwidth of DRAs with heterogeneous dielectric can be attributed to a decreased

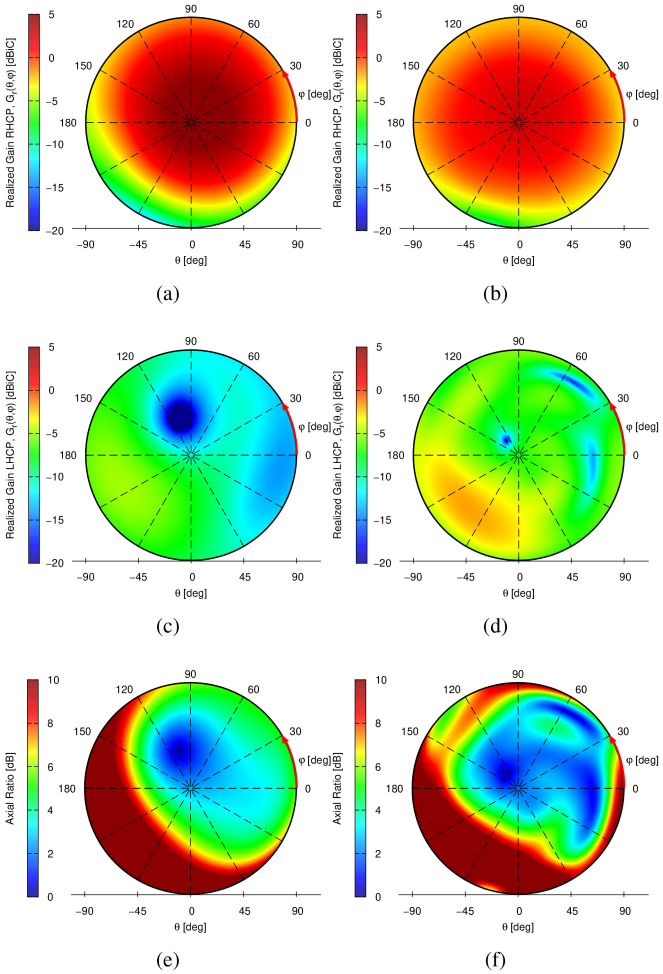

FIGURE 15. RHCP realized gain (a,b), LHCP realized Gain (c,d) and axial ratio (e,f), simulation (left) and measurement (right) results of the inhomogeneous DRA with a linear permittivity profile along the vertical axis at E1 center frequency (1.575 GHz).

coupling between the two coaxial feeds of the DRAs. The physical reason for the mitigated feed-coupling seems to be a decreased dielectric permittivity in the DRAs resonating body between both feeding points. One drawback of the inhomogeneous DRAs is their increased complexity in manufacturing and, for the DRA-IHZ only, the increased volume compared to the homogeneous version. Another potential issue is that this approach is challenging to scale to higher frequencies. The unit-cell size needs to be small compared to the design wavelength for the resulting volume to act as an effective medium but at the same time big enough to be compatible with the employed manufacturing process.

VI. CONCLUSION

This work accomplishes two goals. For the first time in literature, it describes the design and additive manufacturing of an artificial dielectric volume with a continuous linear variation of its relative permittivity and applies such permittivity profiles to improve the performance of probe-fed dielectric resonator antennas. This is achieved by utilizing a dielectric unit cell with face-centered cubic symmetry that is created via the superposition of spatial harmonics. The individual spatial harmonics are used in the powerful SVL algorithm to synthesize a volume with continuously changing volumetric fill-fraction that is then manufactured with a single high-permittivity material in a fused deposition modeling process. Two inhomogeneous DRAs with linear varied permittivity profiles along their radial and vertical axis, and one homogeneous DRA for comparison. The choice of the manufactured permittivity profiles in this work was driven by simplicity in their description rather than optimization constraints. Nevertheless, both inhomogeneous DRAs show mitigated coupling between the feed ports leading to improved realized gain and axial ratio values at the design frequency. These benefits are demonstrated with both numerical simulations and measurements, validating the design and simulation approach proposed. The presented approach to continuously linearly sweep the permittivity profile of dielectric volumes is applicable to DRAs. However, the same technique can be applied to design DRAs with inverse linear or even nonlinear profiles, which shall be addressed in future research. Furthermore, this approach can be applied in numerous other ways, for example, to engineer flat lenses or to introduce tapers in dielectric waveguides without changing their geometry.

REFERENCES

[1] J. L. Volakis, *Antenna Engineering Handbook*. 4th ed. New York, NY, USA: McGraw-Hill Professional, 2007, ch. 17.

[2] S. Keyrouz and D. Caratelli, "Dielectric resonator antennas: Basic concepts, design guidelines, and recent developments at millimeter-wave frequencies," *Int. J. Antennas Propag.*, vol. 2016, Sep. 2016, Art. no. 6075680.

[3] S. Caizzone, G. Buchner, and W. Elmarissi, "Miniaturized dielectric resonator antenna array for GNSS applications," *Int. J. Antennas Propag.*, vol. 2016, pp. 1–10, 2016, doi: 10.1155/2016/2564087.

[4] A. Petosa and A. Ittipiboon, "Dielectric resonator antennas: A historical review and the current state of the art," *IEEE Antennas Propag. Mag.*, vol. 52, no. 5, pp. 91–116, Oct. 2010, doi: 10.1109/MAP.2010.5687510.

[5] B. Mukherjee, P. Patel, and J. Mukherjee, "A review of the recent advances in dielectric resonator antennas," *J. Electromagn. Waves Appl.*, vol. 34, no. 9, pp. 1095–1158, 2020, doi: 10.1080/09205071.2020.1744484.

[6] R. Cicchetti, E. Miozzi, and O. Testa, "A novel wideband multi-permittivity composite dielectric resonator antenna for wireless applications," in *Proc. IEEE-APS Topical Conf. Antennas Propag. Wireless Commun. (APWC)*, 2016, pp. 70–73, doi: 10.1109/APWC.2016.7738121.

[7] F. Wang, C. Zhang, H. Sun, and Y. Xiao, "Ultra-wideband dielectric resonator antenna design based on multilayer form," *Int. J. Antennas Propag.*, vol. 2019, pp. 1–10, Apr. 2019, doi: 10.1155/2019/4391474.

[8] R. K. Chaudhary, K. V. Srivastava, and A. Biswas, "Variation of permittivity in radial direction in concentric half-split cylindrical dielectric resonator antenna for wideband application," *Int. J. RF Microw. Comput. Aided Eng.*, vol. 25, no. 4, pp. 321–329, 2015, doi: 10.1002/mmce.20865.

[9] R. K. Chaudhary, K. V. Srivastava, and A. Biswas, "Multi-band cylindrical dielectric resonator antenna using permittivity variation in azimuth direction," *Progr. Electromagn. Res.*, vol. 59, pp. 11–20, Aug. 2015, doi: 10.2528/PIERC15070708.

[10] R. K. Chaudhary, V. V. Mishra, K. V. Srivastava, and A. Biswas, "Multi-layer multi-permittivity dielectric resonator: A new approach for improved spurious free window," in *Proc. 40th Eur. Microw. Conf.*, Paris, France, 2010, pp. 1194–1197, doi: 10.23919/EUMC.2010.5617151.

[11] F. P. Chietera, R. Colella, and L. Catarinucci, "Dielectric resonators antennas potential unleashed by 3D printing technology: A practical application in the IoT framework," *Electronics*, vol. 11, no. 1, p. 64, Dec. 2021, doi: 10.3390/electronics11010064.
[12] V. Basile et al., "Design and manufacturing of super-shaped dielectric resonator antennas for 5G applications using stereolithography," *IEEE Access*, vol. 8, pp. 82929–82937, 2020, doi: 10.1109/ACCESS.2020.2991358.
[13] S. P. Hehenberger, W. Elmarissi, and S. Caizzone, "Design and installed performance analysis of a miniaturized all-GNSS bands antenna array for robust navigation on UAV platforms," *Sensors*, vol. 22, no. 24, p. 9645, Dec. 2022, doi: 10.3390/s22249645.
[14] C. D. Morales, C. Morlaas, A. Chabory, R. Pascaud, M. Grzeskowiak, and G. Mazingue, "3D-printed ceramics with engineered anisotropy for dielectric resonator antenna applications," *Electron. Lett.*, vol. 57, no. 18, pp. 679–681, Aug. 2021, doi: 10.1049/ell2.12234.
[15] Z. X. Xia, K. W. Leung, and K. Lu, "3-D-printed wideband multi-ring dielectric resonator antenna," *IEEE Antennas Wireless Propag. Lett.*, vol. 18, no. 10, pp. 2110–2114, Oct. 2019, doi: 10.1109/LAWP.2019.2938009.
[16] P. Nayeri and G. Brennecka, "Wideband 3D-printed dielectric resonator antennas," in *Proc. IEEE Int. Symp. Antennas Propag. USNC/URSI Nat. Radio Sci. Meeting*, 2018, pp. 2081–2082, doi: 10.1109/APUSNCURSINRSM.2018.8608331.
[17] C. Yang, Y. Xiao, and K. W. Leung, "A 3D-printed wideband multilayered cylindrical dielectric resonator antenna with air layers," in *Proc. IEEE Asia–Pacific Microw. Conf. (APMC)*, 2020, pp. 561–563, doi: 10.1109/APMC47863.2020.9331456.
[18] Q. Lamotte et al., "Multi-permittivity 3D-printed ceramic dual-band circularly polarized dielectric resonator antenna for space applications," in *Proc. 15th Eur. Conf. Antennas Propag. (EuCAP)*, 2021, pp. 1–5, doi: 10.23919/EuCAP51087.2021.9411245.
[19] J. W. Allen and B.-I. Wu, "Design and fabrication of an RF GRIN lens using 3D printing technology," in *Proc. Terahertz, RF, Millimeter, Submillimeter-Wave Technol. Appl. VI*, San Francisco, CA, USA, 2013, Art. no. 86240V, doi: 10.1117/12.2000708.
[20] R. C. Rumpf and J. Pazos, "Synthesis of spatially variant lattices," *Opt. Exp.*, vol. 20, no. 14, pp. 15263–15274, 2012, doi: 10.1364/OE.20.015263.
[21] A. Goulas et al., "The impact of 3D printing process parameters on the dielectric properties of high permittivity composites," *Designs*, vol. 3, no. 4, p. 50, Nov. 2019, doi: 10.3390/designs3040050.
[22] S. P. Hehenberger, S. Thurner, S. Caizzone, and A. G. Yarovoy, "Broadband effective permittivity simulation and measurement techniques for 3D-printed dielectric crystals," early access, Mar. 30, 2023, doi: 10.1109/TMTT.2023.3259479.
[23] S. Zhang, C. C. Njoku, W. G. Whittow, and J. C. Vardaxoglou, "Novel 3D printed synthetic dielectric substrates," *Microw. Opt. Technol. Lett.*, vol. 57, no. 10, pp. 2344–2346, Oct. 2015, doi: 10.1002/mop.29324.
[24] S. P. Hehenberger, A. P. T. Adithyababu, and S. Caizzone, "Effective permittivity measurement of 3D-printed dielectric crystals," in *Proc. 16th Eur. Conf. Antennas Propag. (EuCAP)*, 2022, pp. 1–5, doi: 10.23919/EuCAP53622.2022.9769370.
[25] V. A. Markel, "Introduction to the Maxwell Garnett approximation: Tutorial," *J. Opt. Soc. America A*, vol. 33, no. 7, p. 1244, Jul. 2016, doi: 10.1364/JOSAA.33.001244.
[26] M. I. Mishchenko, J. M. Dlugach, and L. Liu, "Applicability of the effective-medium approximation to heterogeneous aerosol particles," *J. Quant. Spectrosc. Radiat. Transf.*, vol. 178, pp. 284–294, Jul. 2016, doi: 10.1016/j.jqsrt.2015.12.028.
[27] K. M. Leung and Y. F. Liu, "Photon band structures: The plane-wave method," *Phys. Rev. B, Condens. Matter*, vol. 41, no. 14, pp. 10188–10190, May 1990, doi: 10.1103/PhysRevB.41.10188.
[28] C. R. Garcia et al., "3D printing of anisotropic metamaterials," *Progr. Electromagn. Res. Lett.*, vol. 34, pp. 75–82, Aug. 2012.
[29] Z. Larimore, S. Jensen, P. Parsons, B. Good, K. Smith, and M. Mirotznik, "Use of space-filling curves for additive manufacturing of three dimensionally varying graded dielectric structures using fused deposition modeling," *Addit. Manuf.*, vol. 15, pp. 48–56, May 2017, doi: 10.1016/j.addma.2017.03.002.
[30] R. K. Mongia and P. Bhartia, "Dielectric resonator antennas—A review and general design relations for resonant frequency and bandwidth," *Int. J. Microw. Millim.-Wave Comput.-Aided Eng.*, vol. 4, no. 3, pp. 230–247, Jul. 1994, doi: 10.1002/mmce.4570040304.

SIMON P. HEHENBERGER (Student Member, IEEE) received the B.Sc. and M.Sc. degrees in electronics and information technology from Johannes Kepler University in 2017 and 2020, respectively. During his studies, he focused on high-frequency systems and radar while completing his master thesis about the design, simulation, and test of a fully functional FMCW-MIMO radar system with non-uniform arrays and substrate integrated waveguides. In 2020, he joined the Institute for Communication and Navigation of the German Aerospace Center, where he works on miniaturized dielectric resonator antennas, arrays, and methods for array decoupling with a focus on satellite navigation applications. In 2021, he became an external Ph.D. student with the Microwave Sensing, Signals, and Systems Group, TU Delft. In his Ph.D. project, he explores the potential of additive manufacturing with respect to high-frequency components and antenna systems.

STEFANO CAIZZONE (Member, IEEE) received the M.Sc. degree in telecommunications engineering and the Ph.D. degree in geoinformation from the University of Rome Tor Vergata, Rome, Italy, in 2009 and 2015, respectively. Since 2010, he has been with the Antenna Group, German Aerospace Center, where he has been responsible for the development of innovative miniaturized antennas. Since July 2020, he has been leading the Antenna Systems Group. His main research interests concern small antennas for satellite navigation, controlled radiation pattern antennas for robust satellite navigation, high-performance antenna design for precise satellite navigation, antenna arrays for satellite communication, and installed performance analysis.

ALEXANDER G. YAROVOY (Fellow, IEEE) received the Diploma degree (Hons.) in radiophysics and electronics, the Candidate of Sciences (Physics and Mathematics) degree in radiophysics, and the Doctor of Sciences (Physics and Mathematics) degree in radiophysics from Kharkov State University, Kharkiv, Ukraine, in 1984, 1987, and 1994, respectively. In 1987, he joined the Department of Radiophysics with Kharkov State University as a Researcher, where he became a Full Professor in 1997. From September 1994 to 1996, he was with the Technical University of Ilmenau, Germany, as a Visiting Researcher. Since 1999, he has been with the Delft University of Technology, The Netherlands, where he has been leading the Chair of Microwave Sensing, Systems and Signals since 2009. He has authored and coauthored more than 500 scientific or technical papers, seven patents and 14 book chapters. His main research interests are in high-resolution radar, microwave imaging, and applied electromagnetics (in particular, UWB antennas). He is the recipient of the European Microwave Week Radar Award for the paper that best advances the state-of-the-art in radar technology in 2001 (together with L.P. Ligthart and P. van Genderen) and in 2012 (together with T. Savelyev). In 2010, together with D. Caratelli, he got the Best Paper Award of the Applied Computational Electromagnetic Society. He served as the General TPC Chair of the 2020 European Microwave Week, as the Chair and the TPC chair of the 5th European Radar Conference 2008, as well as the Secretary of the 1st European Radar Conference 2004. He also served as the Co-Chair and the TPC chair of the Tenth International Conference on GPR 2004. He serves as an Associate Editor of the IEEE TRANSACTION ON RADAR SYSTEMS. From 2011 to 2018, he served as an Associate Editor of the *International Journal of Microwave and Wireless Technologies*. From 2008 to 2017, he served as the Director of the European Microwave Association.